

JGR Solid Earth

RESEARCH ARTICLE

10.1029/2020JB020671

Key Points:

- We report the results of rock magnetic properties and backscattered electron investigations in a profile through a subduction splay fault
- Enhanced magnetic mineral diagenesis in two slip zones resulted in the neoformation of iron-sulfide minerals
- We suggest that the accumulation and fault parallel transport of reactants in fracture zones allowed anaerobic methane oxidation to occur

Correspondence to:

A. Greve,
a.greve@uu.nl

Citation:

Greve, A., Kars, M., & Dekkers, M. J. (2021). Fluid accumulation, migration and anaerobic oxidation of methane along a major splay fault at the Hikurangi subduction margin (New Zealand): A magnetic approach. *Journal of Geophysical Research: Solid Earth*, 126, e2020JB020671. <https://doi.org/10.1029/2020JB020671>

Received 27 JUL 2020
Accepted 11 JAN 2021

© 2021. The Authors.

This is an open access article under the terms of the [Creative Commons Attribution License](#), which permits use, distribution and reproduction in any medium, provided the original work is properly cited.

Fluid Accumulation, Migration and Anaerobic Oxidation of Methane Along a Major Splay Fault at the Hikurangi Subduction Margin (New Zealand): A Magnetic Approach

Annika Greve¹ , Myriam Kars² , and Mark J. Dekkers¹ 

¹Paleomagnetic Laboratory 'Fort Hoofddijk', Department of Earth Sciences, Utrecht University, The Netherlands,

²Center for Advanced Marine Core Research, Kochi University, Nankoku, Japan

Abstract Understanding the locus of fluid flow along thrust and splay faults is important to understand the hydraulic properties of accretionary systems and fault mechanics. Here, we use rock magnetic techniques in combination with backscattered electron imaging to depict the locus of enhanced magnetic mineral alteration within the Pāpaku fault, an active splay fault of the subduction interface at the northern Hikurangi Margin. The Pāpaku fault was cored at Site U1518 during Expedition 375 of the International Ocean Discovery Program and we report room temperature magnetic parameters, complemented by first-order reversal and thermomagnetic curves in the depth interval 250–400 m below seafloor (mbsf). The ~60-m wide Pāpaku fault zone comprises two main slip zones, referred to as the upper main brittle (304–321 mbsf) and lower subsidiary (351–361 mbsf) fault zones, and an intervening zoned, termed the lower ductile deformation zone. Two narrow zones, at the top of the main brittle fault zone, and one in a sand-rich interval above the subsidiary fault zone, experienced enhanced magnetic mineral diagenesis, which resulted in the recrystallization of ferrimagnetic greigite to paramagnetic pyrite. We propose that secondary magnetic mineral diagenesis was driven by anaerobic methane oxidation within these intervals, which occurs in the presence of methane and sulfate. We relate the observed changes to the fault parallel transport of fluids which is restricted to two damage zones. Overlying compacted and clay-rich sediments likely act as a barrier to upward advective flow through the fault zone and into the hanging wall.

1. Introduction

The production, presence and migration of fluids in fore-arc regions are fundamental to the distribution and advection of heat (Fagereng & Ellis, 2009). Mineral diagenesis, the formation and dissipation of methane hydrate and metamorphism at depth control the geochemistry of pore-fluids (Kastner et al., 2014; D. M. Saffer & Srean, 2003; Torres et al., 2004). Pore-fluid pressure counteracts hydrostatic stress, and thus is thought to weaken the frictional stability of the sediments and the mechanical strength of fault zones (Ellis et al., 2015; Kastner et al., 2014; Saffer, 2015; Saffer & Tobin, 2011; Srean et al., 2009; Skarbek & Saffer, 2009). A major source of fluids lies near the deformation front of accretionary margins, where soft and porous sediments of the incoming plate are compacted and excess pore-fluid is released (e.g., Kuehn et al., 2019; G. F. Moore et al., 2011; J. C. Moore & Vrolijk, 1992; Taira et al., 1992). Splay- and thrust faults are key conduits that enable drainage of excess expelled fluids from décollement zones and the accretionary wedge. Dilated conduits, in particular brittle structures, increase permeability (Crutchley et al., 2010; Fitts & Brown, 1999). Evidence for these processes is available from geochemical measurements conducted on gas expelled along surface seeps, or from pore-water extracted from cored sediments (Aharon & Fu, 2003; Suess, 2010). Their spatial configuration has important implications for fault zone mechanics (D. M. Saffer & Tobin, 2011). Cored sediments are only available in very limited amounts, and pore-fluid compositions are typically determined with one sample per 5–10 m (see, e.g., Wallace et al., 2019). This wide sample spacing precludes pinpointing the fluid flux loci along young and shallow subduction thrusts.

Rock magnetic techniques have recently gained interest due to their ability to provide information on fluid/gas migration and accumulation, frictional heating processes, shear along fault-planes and soft-sediment deformation in surrounding lithologies (e.g., Chen et al., 2019; Musgrave et al., 2019; Parés, 2015; Yang

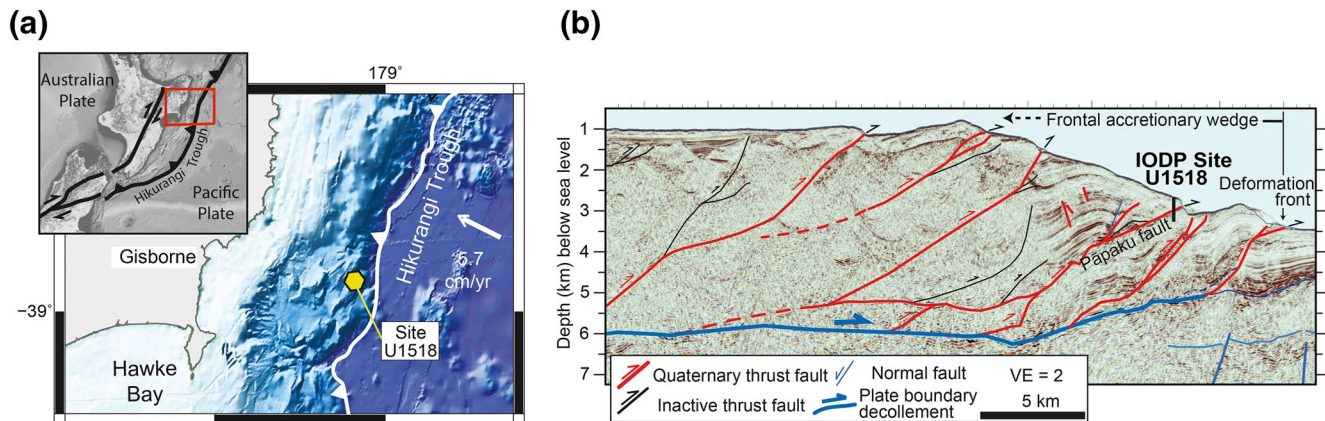


Figure 1. (a) Location and geotectonic setting of the Hikurangi subduction margin and the New Zealand plate boundary (inset). Displayed in the bathymetric map of the northern Hikurangi subduction margin are also the deformation front, IODP Site U1518 and the relative plate convergence vector. (b) Seismic cross section of the frontal accretionary wedge near the drilling transect of IODP Expedition 375, including interpretation after Barker et al. (2018). The location of IODP Site U1518 and trace of the Pāpaku fault are indicated. Figure modified from (Fagereng et al., 2019; Greve et al., 2020). IODP, International Ocean Discovery Program.

et al., 2013). Rock magnetic experiments are rapid, and require little sample material only. So, they can be conducted in higher resolution than more conventional geochemical investigations. Next to detrital iron (oxy) (hydr)oxides, authigenically formed magnetic minerals, particularly greigite (Fe_3S_4), prevail in rapidly accumulated sediment. En route to pyrite (FeS_2) formation, the intermediate sulfides (including greigite) may be preserved in case of a favorable iron to sulfur balance. Sufficient sulfide to complete pyrite formation is often not available in rapidly accumulating sediment (e.g., Roberts et al., 2011). The magnetic minerals thus constitute a probe of past temperature and fluid flow because they are sensitive to heating and/or prevailing redox conditions. These conditions are modified during slip and fluid flux (Chen et al., 2019).

In this paper, we discuss meter scale anomalies in the magnetic behavior of sediments sampled throughout the Pāpaku fault zone, which is a frontal splay fault near the deformation front of the Hikurangi Subduction Margin, New Zealand (Figure 1). The sediments were recovered at Site U1518 during Expedition 375 of the International Ocean Discovery Program (IODP). The site is located in a region that is known to host shallow slow-slip earthquakes (Wallace et al., 2016), although it is yet unclear how shallow thrust faults contribute to the dissipation of seismic energy (Wallace et al., 2016). The results of the present study provide evidence for the migration of methane-bearing fluids along spatially limited pathways, thus providing crucial information needed to better understand the permeability structure, mechanic properties, and evolution of shallow thrust faults.

2. Background

2.1. Site Details and Shipboard Investigations

The Pāpaku fault zone is a roughly westward dipping, shallow subduction thrust which traces Earth's surface only a few kilometers away from the deformation front of the northern Hikurangi subduction margin in north-east New Zealand (Figure 1a). It roots into the main plate interface décollement ca. 2 km further to the west (Figure 1b) (Bell et al., 2014; Fagereng et al., 2019; Saffer et al., 2017; Wallace et al., 2019). Hole U1518F of IODP Expedition 375 ($38^\circ 51.57'S$, $178^\circ 53.76'E$, water depth: 2,626.1 mbsl) cored hanging wall, fault zone and footwall sequences up to a maximum depth of 492.3 meters below sea floor (mbsf). The average core recovery in the studied intervals is ca. 43%. The core recovery in the fault zone and footwall is somewhat lower (Figure 2a). In these intervals, less cohesive sand-rich intervals and fractured material led to increased destruction of core material during the drilling process. Data sets from shipboard investigations, including geochemical analysis, core description and physical properties measurements provide a wealth of information on fault zone architecture and sediment mechanical properties. Shipboard core descriptions

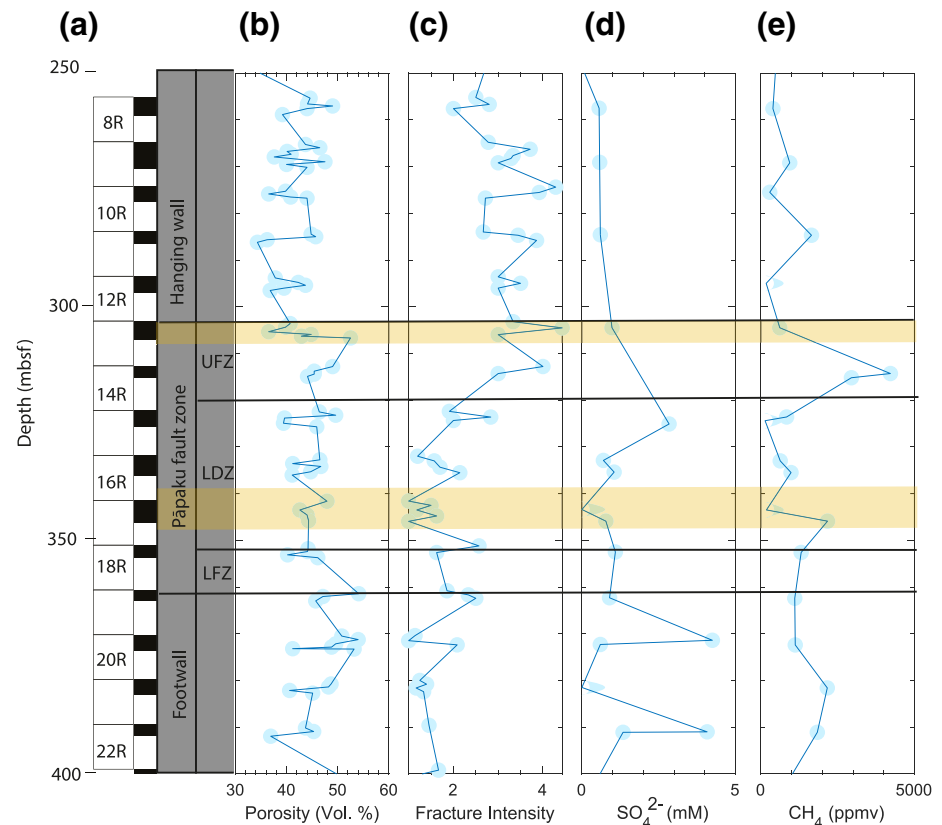


Figure 2. Shipboard downcore properties. Displayed in (a) are the core IDs and recovery of core-material (black intervals: core recovered); the main structural domains (cf., Wallace et al., 2019). UFZ—upper main brittle fault zone, LDZ—lower ductile deformation zone, LFZ—lower subsidiary fault zone. The shaded intervals in yellow correspond to intervals in which anomalous rock magnetic properties were measured (cf., Figure 4, top: Anomaly A, bottom: Anomaly B). (b) Downcore variations of discrete sample porosity; (c) fracture intensity, an index number which describes the relative abundance of fractures over 10 cm intervals, averaged per core section (1: long unfractured section of core, 5: intensely brecciated zone); (d) sulfate concentration (uncorrected for drilling fluid contamination); and (e) methane concentration. For data, details and methods the reader is referred to Wallace et al. (2019).

included the determination of porosity (Figure 2b) and the estimation of the fracture intensity (Figure 2c), which quantifies the density of open fractures within the core-sections recovered (Wallace et al., 2019).

Shipboard investigations also included the analysis of key pore-water solutes, including sulfate (Figure 2d), chloride, and dissolved metal ions (Wallace et al., 2019). For these analyses ca. 20–40-cm long segments were removed from every 5–10 m of core recovered through the hanging- and footwall. Through the fault zone interval one sample every 7–20 m was processed. Pore-water was squeezed out of the sediment using a hydraulic press, and key solutes measured. Additional gas chromatography was conducted on two head-space samples per core to measure hydrocarbon gases including methane (cf. Figure 2e; ca. one sample every 5 m, refer to Wallace et al., 2019 for details).

2.2. Lithostratigraphy, Fracture Density, Porosity, and Pore-Fluid Chemistry

Hole U1518F cored the Pāpaku fault zone between 304.5 and 361.7 mbsf. The roughly 60-m thick fault zone forms the active, structural boundary between consolidated and heavily deformed hanging wall sediments which are overthrust over younger and less consolidated footwall sediments (Fagereng et al., 2019; Greve et al., 2020; Morgan et al., 2020; Wallace et al., 2019).

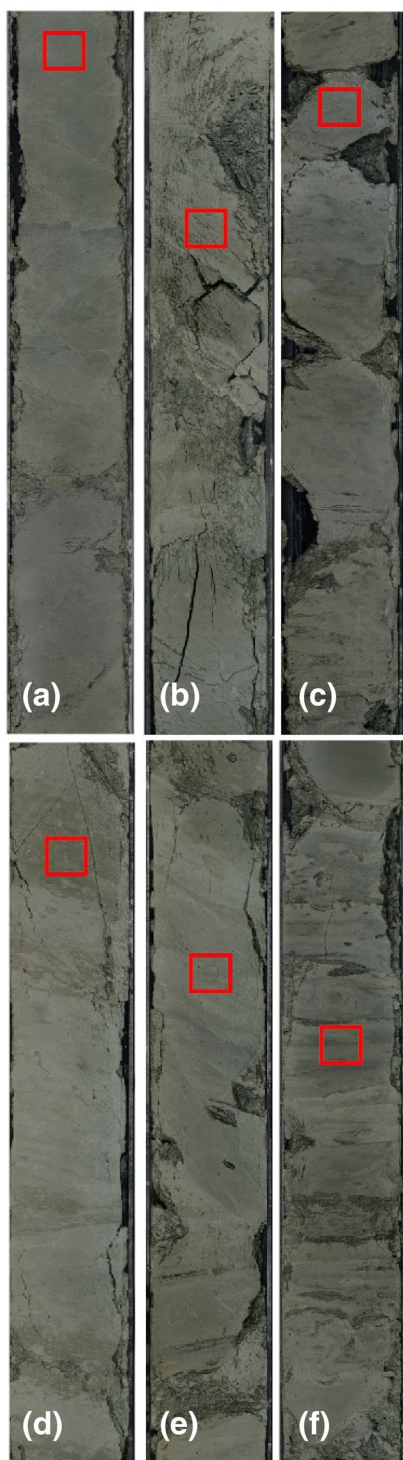


Figure 3. Examples of core photographs; the red rectangles correspond to the locations where samples for first-order reversal curve (FORC) measurements and backscattered electron (BSE) imaging were taken from (a) hanging wall, 303.5 mbsf, (b) upper main brittle fault zone, Anomaly “A,” 304.7 mbsf, (c) lower ductile deformation zone, 322.8 mbsf, (d) central fault zone, Anomaly “B,” 342.1 mbsf, (e) lower ductile deformation zone, Anomaly “B,” 345.1 mbsf, (f) lower subsidiary fault zone, 353 mbsf.

The sediments recovered throughout hanging wall, fault zone, and footwall consist of Pleistocene mudstone sequences that are sparsely interbedded with thin graded silt- and sandstone layers. The frequency of sand- and siltstone beds increases near the bottom of the fault zone and through the footwall, where contorted, sand-rich intervals have been interpreted as gravity driven mass-transport deposits that contain coarser grained clastic and volcanoclastic material (Figure 3f). The lower hanging wall is pervasively deformed. It yields variable bedding tilts and localized zones of overturned bedding. Folding is accompanied with brittle fracturing, and the fracture intensity peaks in a fold hinge zone at ca. 275 mbsf (Figure 2c). Between 304 and 361 mbsf is the Pāpaku fault. A detailed description of fault zone architecture and deformation was provided by (Fagereng et al., 2019; Wallace et al., 2019). Fagereng et al. (2019) subdivided the ~60-m thick fault zone into three main domains: (i) the upper main brittle fault zone, (ii) the lower ductile deformation zone, and (iii) the lower subsidiary fault zone. The upper main brittle fault zone (304–321 mbsf) was defined based on an abrupt increase in brittle fracturing (Figure 2c). Brittle fractures coexist and often overprint older ductile deformation features. Brittle fracturing in the lower hanging wall and the upper main fault zone often damaged primary sediment features and bedding. In contrast, the deformation decreases throughout an intervening zone between 322 and 351 mbsf, referred to as lower ductile deformation zone. A second zone of higher intensity deformation, here referred to as the lower subsidiary fault zone, was identified between 351 and 361 mbsf (Wallace et al., 2019).

Biostratigraphic investigations identified an age inversion near the top of the upper main brittle fault zone suggesting that the majority of the fault zone interval is located within the younger footwall rock (Wallace et al., 2019). This observation is coherent with the finding of magnetic fabric analyses (Greve et al., 2020), which indicate that strain is decoupled between hanging- and footwall sequences near the top of the upper main fault.

3. Methods

3.1. Rock Magnetic Analysis

Samples for rock magnetic analyses were extracted from working-half sections by pushing 7 cm³ “Natsuhara-Giken” sample cubes into the sediment, while avoiding intervals that were affected by localized deformation or mass transport deposits (i.e., sand, silt-rich intervals, and volcanic ash flows). For this study 63 samples were collected from the interval 250–400 mbsf in Hole U1518F, using a spacing of about 1 m of core recovered. Anisotropy of magnetic susceptibility was measured using an AGICO KLY-4 Kappa Bridge at the Japan Agency for Marine-Earth Science and Technology in Yokosuka (Japan) and mean magnetic susceptibility (χ) extracted. These results were previously reported in Greve et al. (2020). All other magnetic measurements were conducted at the Center for Advanced Marine Core Research in Nankoku (Japan). Samples were first measured for their natural remanent magnetization (NRM), subsequently demagnetized by static alternating fields (AF) up to 80 mT and afterward given an anhysteretic remanent magnetization (ARM) in a direct current (DC) bias field of 50 μ T with a peak AF of 80 mT. Acquired

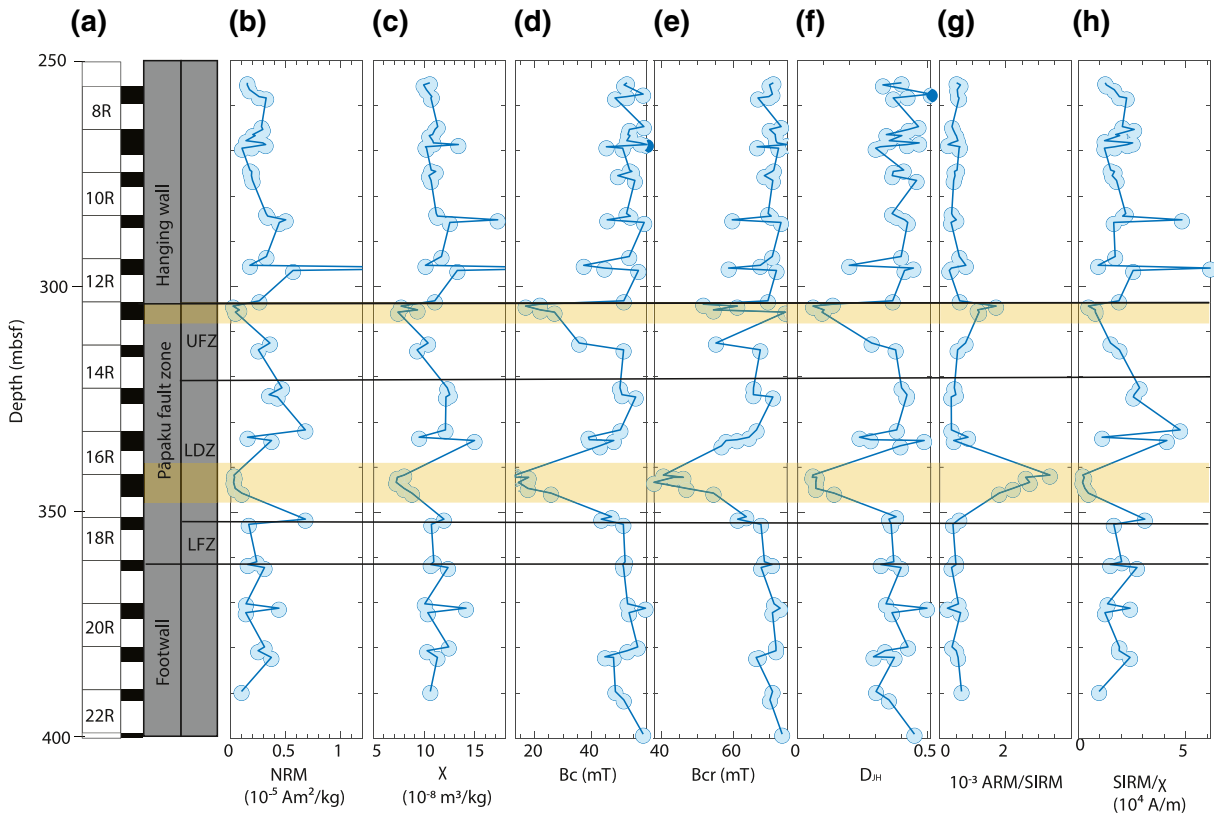


Figure 4. Downcore rock magnetic parameters. (a) Core IDs and recovery of core-material (black intervals: core recovered) and structural domains (cf., Figure 2). (b) The Natural Remanent Magnetization (NRM). (c) Bulk magnetic susceptibility (χ). (d) The magnetic coercivity (B_c). (e) The coercivity of remanence (B_{cr}). (f) D_{JH} , which is the ratio of the hysteresis parameters $D_{JH} = (M_{rs}/M_s)/(B_{cr}/B_c)$ (Housen & Musgrave, 1996). (g) The ratio between the anhysteretic remanent magnetization (ARM) divided by the saturation isothermal remanent magnetization (SIRM). (h) The ratio between SIRM and χ .

ARM was measured using a 2G SQUID cryogenic pass-through magnetometer. A selection of samples was subjected to partial ARM acquisition (pARM) in AF fields that were increased in 5 mT steps to a peak field of 80 mT, while applying a 50 μ T DC bias field.

Further analyses included the measurement of isothermal remanent magnetization (IRM) using a Nat-suhara Giken spinner magnetometer following exposure of the samples to a 1.2 T applied field using a MMPM1 pulse magnetizer. At this field samples were considered saturated and the acquired remanence will be referred to as saturation isothermal remanent magnetization (SIRM) in the following text. Subsequently, after the measurements on the cubes, 150–300 mg of material was carefully removed from each cube, covered, dried overnight in air at room temperature and packed into gelatin capsules for additional analyses. Magnetic hysteresis, backfield curves and IRM acquisition curves were measured using a Princeton Measurements Corporation vibrating sample magnetometer with a 1 T maximum field. Hysteresis and backfield remanence parameters (saturation magnetization M_s , saturation remanent magnetization M_{rs} , coercivity B_c , and remanent coercivity B_{cr}) were calculated following automated slope correction (saturation is assumed at 70% of the saturating field). These parameters effectively describe the shape of hysteresis loops, which is linked to dominant magnetic mineralogy and magnetic grain-size in a sample. We summarize all four parameters into the ratio $D_{JH} = (M_{rs}/M_s)/(B_{cr}/B_c)$, which has been shown to increase with increasing iron-sulfide content in mixed assemblages of iron oxides and diagenetically produced iron sulfides (Housen & Musgrave, 1996).

To further investigate magnetostatic interactions we measured first-order reversal curves (FORCs; Pike et al., 1999; Roberts et al., 2014, 2000) on a selection of samples from the hanging wall, the fault zone and the footwall sequences. Each measurement sequence included the measurement of 150 FORCs with an averaging time of 100 ms and a field increment of 2 mT. The FORC diagrams were processed using the

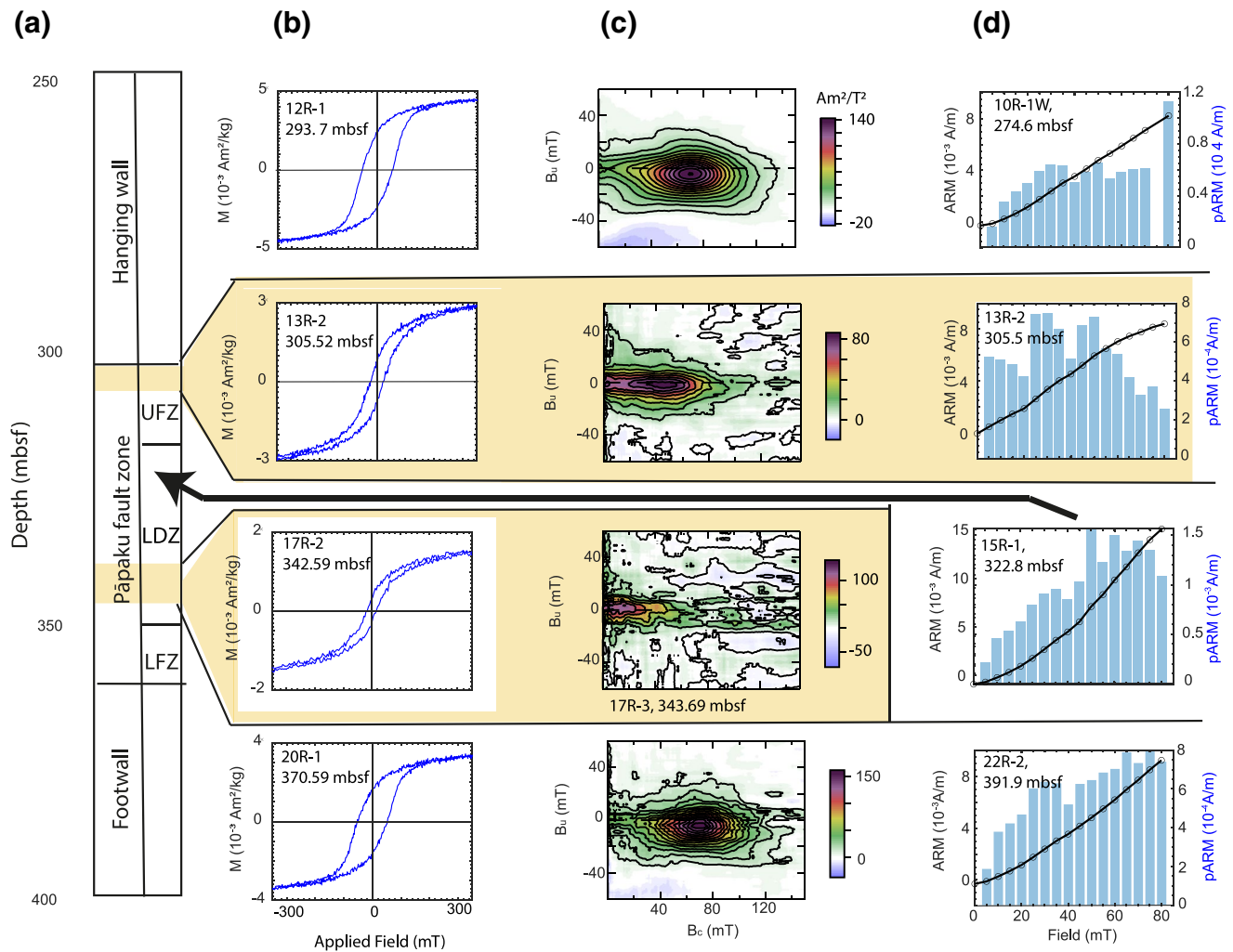


Figure 5. Representative rock magnetic properties of samples from hanging- and footwall (top and bottom rows, respectively) and from two intervals within the Pāpaku fault zone that yield anomalous magnetic properties. (a) Structural domains of the Pāpaku fault zone, where UFZ—upper main brittle fault zone, LDZ—lower ductile deformation zone, LFZ—lower subsidiary fault zone. (b) Hysteresis loops after slope correction (saturation field of 1 T). (c) First-order reversal curve (FORC) diagrams. (d) Anhysteretic remanent magnetization (ARM) acquisition curves (black line), and partial ARM (pARM) acquired at each treatment step (light blue columns). Sample identifiers and depth information are displayed in the top left corner of the hysteresis loop panels. See text for details.

FORCinel software (Harrison & Feinberg, 2008) with the VARIFORC protocol of Egli (2013). First point and lower branches were subtracted. Thermomagnetic curves were measured in air using a modified horizontal translation Curie Balance (noise level 5×10^{-9} Am²) (Mullender et al., 1993) at Utrecht University (The Netherlands). To detect the onset of thermochemical alteration samples were subjected to heating and cooling cycles, up to increasingly elevated peak temperatures of 250°C, 350°C, 450°C, 520°C, 620°C and 700°C.

3.2. Backscattered Electron Imaging

Seven samples including two from Anomalies “A” and “B” each, and three samples from the hanging wall, lower ductile deformation zone and the footwall, respectively, were further investigated using backscattered electron (BSE) imaging. Polished thin sections were prepared from vacuum dried (maximum temperature: 30°C), powdered samples. BSE imaging was conducted at the Department of Earth Sciences at Utrecht University using a JEOL JXA-8530F Electron Microprobe (accelerating voltage: 15 keV).

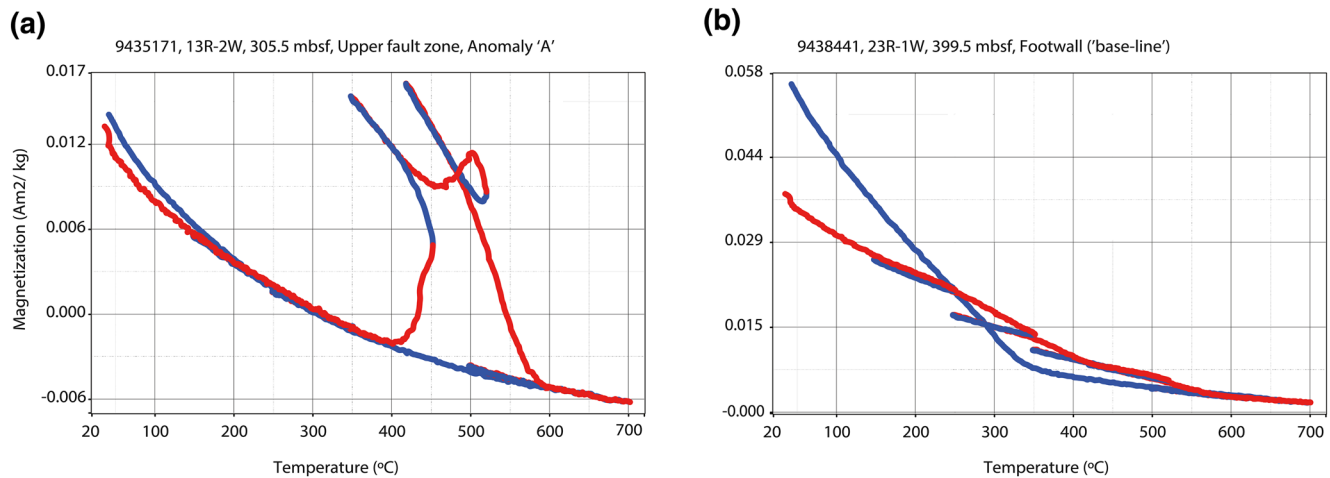


Figure 6. Representative stepwise thermomagnetic curves in air from (a) a sample from Anomaly “A” in the upper fault zone, (b) “base-line” lithology (here: footwall). Sample ID’s, core section and depth information are indicated above each figure. Red = heating segment (heating rate 6°C/min), blue = cooling segment (cooling rate 10°C/min). Peak temperatures of subsequent segments: 250°C, 350°C, 450°C, 520°C, 620°C, 700°C.

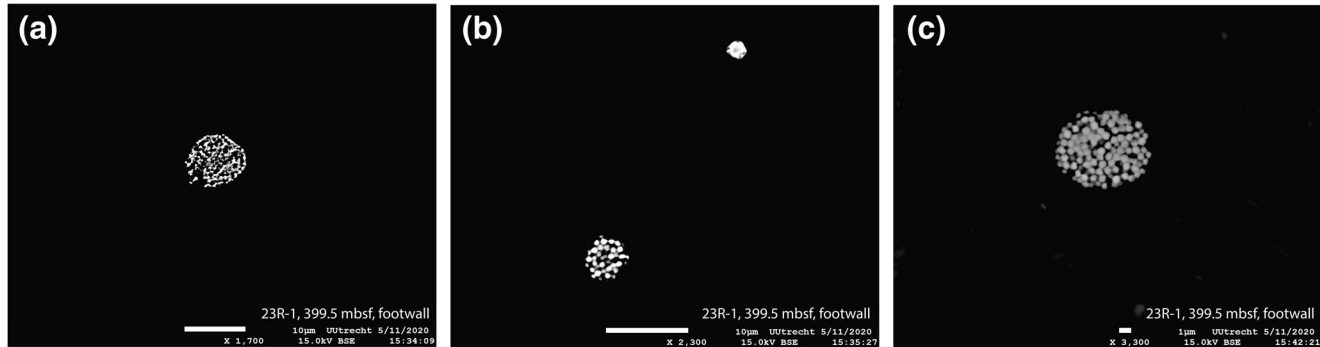
4. Results

4.1. Downhole Trends in NRM, χ , SIRM, and Hysteresis Parameters

Downcore diagnostic magnetic parameters from discrete sample measurements are displayed in Figure 4. The NRM ranges from 2.1×10^{-7} up to 1.4×10^{-5} Am²/kg (Figure 4b) although almost all samples yield NRM intensities around 3.2×10^{-6} Am²/kg (average and standard deviation of hanging- and footwall: $3.21 \times 10^{-6} \pm 3.6 \times 10^{-6}$ Am²/kg, $N = 31$), equivalent to 4.9×10^{-3} A/m when NRM is volume-normalized. The peak intensity was measured on a single sample at ca. 296.3 mbsf. This sample was collected from a more sand- and silt-rich interval, where tectonic deformation resulted in a mixing between hemipelagic sediments and sand/silt-rich gravity deposits. The higher remanence intensity measured on this sample presumably reflects a higher concentration of detrital magnetic minerals. In contrast, in two narrow intervals, between ca. 304–312 mbsf and ca. 334–351 mbsf, sample measurements display remarkably low NRM intensities. These apparent anomalies are reflected in all magnetic measurements discussed throughout this paper. We thus refer to “Anomaly A” for the upper interval between ca. 304–312 mbsf and “Anomaly B” for the lower interval between ca. 334–351 mbsf. All other intervals will be referred to as “base-line” in the remaining discussion.

Magnetic susceptibility χ (Figure 4c) mimics the variations in NRM. It ranges from 5.2 to 13.7×10^{-8} m³/kg, with the lowest values measured within Anomalies “A” and “B,” and the peak value measured on the isolated sample taken from the sand-rich interval. The magnetic coercivity (B_c), the coercivity of remanence (B_{cr}), and the D_{JH} parameter are not affected by the magnetic mineral concentration. Peaks and troughs measured within the anomalous intervals appear much sharper than those recorded by the concentration dependent proxies discussed above (i.e., NRM and χ). Hysteresis loops from the host sediment are open (Figure 5b) with B_c values measured on samples from the hanging- and footwall averaging 52.5 ± 4.7 mT ($N = 39$) (Figure 4d). In contrast, hysteresis loops from Anomalies A and B are much skinnier and display coercivities as low as 13 mT (Figures 5b and 4d). B_{cr} (Figure 4e) averages 70 ± 3.2 mT ($N = 39$) in hanging- and footwall and shows values as low as 37.9 mT within the anomalous intervals. Hanging wall and footwall samples display D_{JH} (Figure 4f) ratios of 0.39 ± 0.06 ($N = 39$), while Anomalies “A” and “B” display two distinct troughs with values as low as 0.056. The ARM/SIRM ratio, sensitive to the magnetic grain-size (Q. Liu et al., 2012; Peters & Dekkers, 2003), displays “base-line” values of $4.9 \times 10^{-4} \pm 1.2 \times 10^{-4}$ ($N = 31$) and two prominent peaks at 1.7×10^{-3} and 3.4×10^{-3} that correspond to Anomalies A and B, respectively (Figure 4g). The SIRM/ χ ratio is sensitive to grain-size and has also shown to increase with the introduction of greigite in diagenetically altered marine sediments (e.g., Larrasoña et al., 2007; Musgrave et al., 2019; Snowball, 1991). It mostly mimics the variations in NRM intensity and χ described above (Figure 4h). Spikes in SIRM/ χ ratio, which are associated with sand- and/or silt-rich intervals obscure the signal of the anom-

Base-line (footwall)



Anomalies A and B

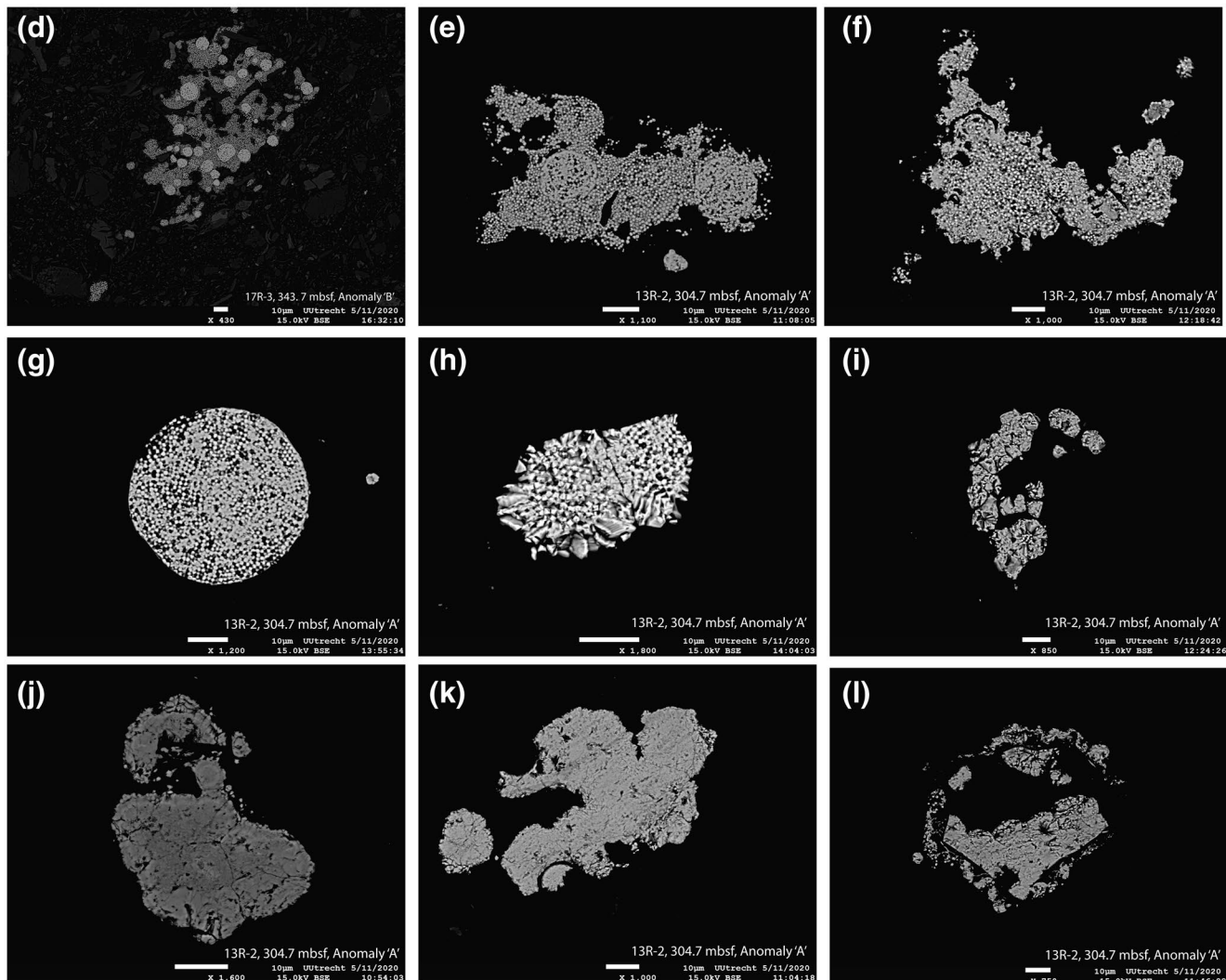


Figure 7. Backscattered electron (BSE) images of representative iron sulfides in four samples from (a–c) base-line sediments, (d–l) two zones that display anomalous magnetic properties (Anomalies “A” and “B”) caused by the recrystallization and neoformation of iron-sulfide minerals. (a–c) Isolated, small (<10 μm) framboids from a footwall sample. (d–f) Polyfamboidal aggregates, each framboid consists of small octahedral iron sulfide grains (probably pyrite). (g) Large, circular framboid (ca. 100 μm diameter). (h–i) Variably recrystallized iron sulfide aggregates. While anhedral crystals form around the rims, small framboids are still visible in the center. (j–l) Fully recrystallized iron sulfide grains.

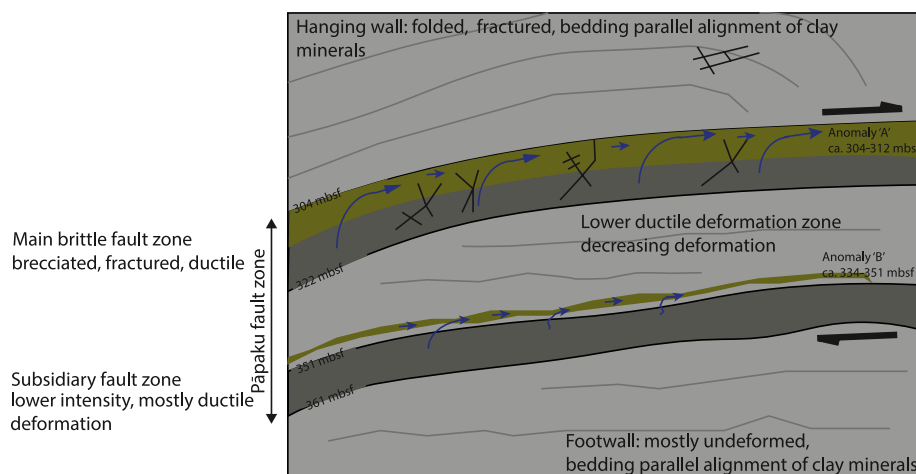


Figure 8. Schematic diagram displaying the main structural domains of the Pāpaku fault zone and inferred fluid migration. In our model we suggest that consolidated hanging wall sediments and compacted, ductilely deformed sediments of the lower ductile deformation zone act as a backstop and result in the accumulation and fault-parallel migration of solutes within two high permeability zones. Anaerobic methane oxidation (AOM) in the presence of methane and sulfate allowed secondary magnetic mineral diagenesis in these intervals (marked in green).

alous intervals. Nevertheless, within Anomalies “A” and “B,” the SIRM/ χ ratio display lower values than in the “base-line” lithology.

4.2. FORC Diagrams, ARM Acquisition, and Thermomagnetic Curves

Differences in the magnetic properties between “base-line” lithology and the two anomalous intervals, Anomalies “A” and “B,” are also reflected in FORC diagrams and thermomagnetic curves. Samples from the hanging wall, footwall and most of the fault zone display FORC density distributions that have closed and concentric contours with a coercivity in between 40 and 90 mT; the highest density is at ~ 70 mT. This is typical of the behavior often observed in samples that contain single domain (SD) greigite (Fe_3S_4) (Roberts et al., 2006; see also Greve et al., 2020). ARM acquisition curves from these horizons display a wide distribution of coercivities that peak above 40 mT (Figure 5d, see also Greve et al., 2020). Thermomagnetic curves (Figure 6b) display slight change in slope at heating temperatures between 250°C and 400°C, which, following heating to 350°, is irreversible. Heating curves display a second decrease in slope at temperatures higher than ca. 525°C. The first is probably caused by the progressive decomposition of greigite upon heating to fine-grained magnetite. The latter loss in magnetization is explained by the oxidation of the newly formed magnetite to hematite (Chang et al., 2008; Dekkers et al., 2000; Krs et al., 1990; Roberts, 1995; van Baak et al., 2016; Vasiliev et al., 2008). Samples from Anomalies “A” and “B” display markedly different FORC and thermomagnetic behavior. FORC diagrams are significantly noisier and display narrow contours along the B_c axis that tail up to 50 mT, and diverge along B_u axis in the low coercivity (0–10 mT) range, typical for mixtures of vortex-state and multidomain sized iron-oxide minerals (Pike et al., 1999; Roberts et al., 2014). pARM acquisition curves also indicate a predominance of lower coercivity magnetic mineral phases. All thermomagnetic curves measured on samples from Anomalies “A” and “B” (e.g., Figure 6a) display a noteworthy and irreversible increase in magnetization at temperatures higher than 400°C, followed by a rapid decay in magnetization upon heating to temperatures between 500°C and 580°C. This behavior has been explained as the oxidation of nonmagnetic pyrite to ferrimagnetic magnetite during heating in past literature (Passier et al., 2001; van Baak et al., 2016; Van Baak et al., 2013). Further oxidation of magnetite to hematite during progressive heating results in lower magnetization measured on cooling curves (Figure 6a). A slightly steeper slope on the heating curves between 250°C and 400°C, which would provide evidence for the coexistence of pyrite and greigite, is not visible. This contrasts markedly with “base-line” samples where such an irreversible decay is clearly present (Figure 6b).

4.3. BSE Observations

We found framboidal aggregates of iron-sulfide minerals in all samples from BSE observations (Figure 7). In samples from “base-line” lithology iron sulfide occurrence is limited to few, small ($<5\ \mu\text{m}$) circular framboids, which were difficult to identify. Each framboid consists of small ($<0.5\ \mu\text{m}$), octahedral, or irregular shaped iron-sulfide grains which display a bright backscatter (Figures 7a–7c). In contrast, the samples from Anomalies “A” and “B” contain a significantly larger abundance of iron-sulfide minerals. These exist as large (up to $400\ \mu\text{m}$ diameter) polyframboidal aggregates (Figures 7d–7f), in which the individual crystals of the various framboids have different grain sizes. Recrystallization and formation of euhedral iron sulfides with sizes $< 5\ \mu\text{m}$ (probably pyrite) is often visible along the rims of individual aggregates (Figures 7h and 7i). Larger ($50\text{--}150\ \mu\text{m}$), irregular shaped iron-sulfide grains (pyrite) which probably formed during progressive recrystallization of preexisting aggregates (Figures 7j–7l). Recrystallization of framboids and formation of euhedral iron-sulfide grains (probably pyrite) in samples from Anomalies “A” and “B” indicate that secondary mineral diagenesis occurred within these intervals. Besides the recrystallization and neof ormation of iron sulfides, this observation would have resulted in the alteration of accessory greigite, originally present in “base-line” lithology, as evidenced from thermomagnetic experiments, to pyrite (see, e.g., Roberts & Weaver, 2005, refer also to discussion). The removal of ferrimagnetic greigite from “base-line” lithology during secondary mineral diagenesis, means that the weak NRM in the anomalous intervals is carried most likely by a few residual iron oxides, for example such that exist as inclusions in dissolution-resistant silicate minerals (Just et al., 2012). This finding provides an explanation for the lower NRM and SIRM values in samples from Anomalies “A” and “B” (Figure 4), and the larger effective magnetic grain-size of residual iron-oxides as evidenced from coercivity, ARM/ χ (Figure 4), FORC diagrams (Figure 5) and the predominance of lower coercivity magnetic mineral phases found in pARM acquisition curves.

5. Discussion

5.1. Downhole Rock Magnetic Variations as a Proxy for Anaerobic Oxidation of Methane Within the Pāpaku Fault

The results of magnetic properties measurements, together with BSE imaging provide compelling evidence that SD sized greigite is the primary remanence carrier throughout most of the studied interval, that is, in the “base-line” sediment. Exceptional are two anomalous intervals (approximately between 304 and 312 mbsf and 334 and 351 mbsf, respectively) within the Pāpaku fault zone that yield a rock magnetic signature distinctively different from the surrounding lithology. This is linked to the enhanced precipitation of iron-sulfide phases (presumably mostly pyrite) and reduction of existing, ferrimagnetic greigite to paramagnetic pyrite in these zones. Alteration of magnetic minerals in shear zones has previously been linked to frictional heating and/or fluid migration (Yang et al., 2020 and references herein). In the following, we discuss possible mechanisms as explanation for the observed changes. Magnetic studies on fault rocks mostly focused on sites that hosted large megathrust earthquakes, such as the Mw 9.0 Tohoku-oki earthquake in 2011 (Yang et al., 2018, 2016) and the Mw 7.9 Wenchuan earthquakes in 2008 (D. Liu et al., 2016), where localized frictional heating temperatures on the principal slip zone are argued to have exceeded 500°C .

Authigenic greigite and pyrite, which were identified here, break down at temperatures as low as 250°C – 350°C and 500°C , respectively (Yang et al., 2020). They usually form at low burial temperatures following early sediment deposition at the sulfate-methane transition zone (SMTZ) where the reaction between dissolved sulfide (mostly from anaerobic methane oxidation [AOM]) and iron (either dissolved or not) results in the progressive reduction of iron-oxide minerals to paramagnetic pyrite (FeS_2) (see, e.g., Chen et al., 2019; Fu et al., 2008; Kars & Kodama, 2015; Larrasoana et al., 2007; Roberts et al., 2011; Roberts & Weaver et al., 2005; Rowan et al., 2009). Greigite (Fe_3S_4) is an intermediate mineral phase in the pyrite formation chain that remains in the sediment if dissolved sulfate is depleted before greigite’s further reduction to pyrite. Rapid sedimentation rates and an associated upward shift of the SMTZ at continental margins favor the preservation of greigite over pyrite formation. However, a change in redox conditions has been widely described to drive enhanced or secondary mineral diagenesis (e.g., Housen & Musgrave, 1996; Larrasoana et al., 2007; Musgrave et al., 2019). Localized enhanced magnetic mineral diagenesis in active deformation zones have previously been linked to fluid flux, methane trapped in high permeability fracture zones (e.g.,

Larrasoana et al., 2007; Musgrave et al., 2019), methane accumulating below low porosity intervals and gas hydrate occurrences (Kars et al., 2019; Kars & Kodama, 2015). Faults are assumed to be the main transport pathway for surface gas seeps along the Hikurangi margin (Faure et al., 2010; Greinert et al., 2010; Lauer & Saffer, 2015; Pettinga, 2003; Watson et al., 2019) and continental margins worldwide (Crutchley et al., 2014; Geersen et al., 2016; Mau et al., 2017; Suess, 2010). Site U1518 lies within the hydrate stability zone, and widespread but cm-thick hydrate accumulations identified within sand- and silt-rich layers led to the conclusion that the vertical flux of methane is largely controlled by diffusive migration (Cook et al., 2020). Gas hydrate formation is a slow and exothermic process that depends on temperature, pressure, methane concentration and solubility in existing pore-water, and geometry of the pore-space available (Collett et al., 2019; Ruppel & Waite, 2020; You et al., 2019). The diffusive transport of methane probably results in its accumulation in brittle, more porous structures within the damage zone of the Pāpaku fault from where it is more favorable to travel in a fault parallel direction. Dissolution in deeper pore-water seeping along high permeability zones would reduce the overall concentration of methane in the pore-fluid which may become undersaturated, thus hampering hydrate formation (e.g., Collett et al., 2019). Continuous and slow seepage of methane rich fluids along the permeable structure of the Pāpaku fault may provide a self-sustaining transport mechanism. For AOM to occur beneath the SMTZ, methane and sulfate are required. Traditionally thought to be sourced from seawater only, increasing evidence suggests that the microbially driven oxidation of pyrite can result in the production of sulfate (see, e.g., Bottrell et al., 2000; Holmkvist et al., 2011; Torres et al., 2015). At Site U1518, an alternative source of sulfate could be from fresh porewater from the underthrust footwall. The SMTZ is located at ~20 mbsf within the upper meters of unconsolidated seafloor sediment in the hanging wall (Wallace et al., 2019), and it thus appears more likely that these soft and unconsolidated sediments were offscraped and frontally accreted rather than incorporated into the accretionary system.

5.2. Fault Permeability Structure

Our results suggest that the migration of methane- and/or sulfate/sulfide and to a minor extent frictional heating at the drill site played a role in the precipitation of pyrite and secondary reduction of existing greigite. Recent results from biomarker thermal maturity analysis indicate elevated paleo-heating temperatures in four discrete, and mm thick intervals through the Pāpaku fault zone, two of which are located within the intervals of the magnetic property anomalies discussed in this paper (Coffey et al., 2021). Short-lived slip events, in association with frictional heating and the migration of co-seismic fluids may thus have resulted in the mobilization of iron and sulfur at the drill site, but were restricted to a narrow, millimeter to centimeter wide zone immediately adjacent to the principal slip zone and thus cannot explain the observed anomalies. In addition, BSE images showed the presence of anhedral pyrite grains and large poly-framboidal growths of iron sulfides within the anomalous intervals. We infer from a mass-balance point of view that their formation is more likely caused by slow AOM that occurs predominantly during interseismic periods.

The two magnetic properties anomalies are located at the top of the upper main brittle fault of the Pāpaku fault zone (Anomaly “A”), and immediately above the lower subsidiary fault (Anomaly “B”). They are separated by the central part of the fault zone, which is an interval with mostly intact, subhorizontal bedding, that is superimposed with few brittle and ductile deformation structures (Figure 8, Wallace et al., 2019). In clay-rich sediments, permeability anisotropy caused by the compaction of clay-rich sediments, fracturing and grain-size differences, influences the direction and locus of fluid flow (Saffer & Tobin, 2011). The majority of advective flow is thought to be concentrated along narrow pathways on thrust and secondary splay-faults (Lauer & Saffer, 2015; Saffer & Tobin, 2011).

We propose that the zonation between sediments that experienced enhanced secondary diagenesis and those that have not, reflect on differences in hydraulic permeability through the fault zone. Anomaly “A” coincides with the upper 8 m of the upper main brittle fault zone, which experienced intensive brecciation, thus forming a more permeable conduit. While at its top Anomaly “A” displays a sharp peak from base-line values to its maximum expression, in its lower portion the magnetic properties more gradually return to base-line values with depth, indicating a progressive increase in greigite content. We suggest that the highest degree of diagenesis coincides with the most prolonged accumulation of solutes at the top of the

main brittle fault zone, where fluids are trapped beneath less permeable hanging wall sediment and forced to migrate in a fault parallel direction (see also Musgrave et al., 2019). At first sight it appears contradictory that Anomaly “A” is capped at the top of the fault zone, even though the lower hanging wall forms a wider and fractured damage zone (Figure 2c). It is noteworthy, however, that the hanging wall preserves bedding, with a near-bedding parallel alignment of clay-fabric (Greve et al., 2020; Wallace et al., 2019), which probably provides a barrier to limit advective flow out of the more permeable main brittle fault zone. The top of the main fault also forms the boundary between overriding hanging- and footwall, which have experienced significantly differing strain (Greve et al., 2020; Fagereng et al., 2019; Morgan et al., 2020). Subhorizontally compacted and ductilely deformed sediments within the center of the fault zone likely provide a barrier that limits the migration of fluid across the fault. Anomaly “B” is located above the lower subsidiary fault zone, and in a sand- and silt-rich interval that, based on shipboard core description, was described as having experienced low intensity deformation only (e.g., Figure 3d). It coincides with the locus of a slip zone identified from thermal maturity analysis (Coffey et al., 2021). Similar to our interpretation of Anomaly “A”, it is possible that shearing was accompanied by the flow and/or accumulation of reducing fluids that produced conditions favorable for the crystallization of iron-sulfide minerals. While it remains difficult to quantify and determine the source of methane and sulfate, the time-scale across which these reactions take place, and thus whether fluids were sourced within the upper accretionary system or whether they traveled from the main décollement, analysis of the results from the deployment of observatories (Wallace et al., 2019) in the fault zone may provide further insight into these processes.

6. Conclusions

The ca. 60 m thick Pāpaku fault zone forms a major and active frontal thrust near the deformation front of the Hikurangi Subduction Margin, New Zealand. It was cored during Expedition 375 of the IODP. Magnetic property measurements in combination with electron microprobe imaging were conducted on one to two samples per meter of core recovered. Two prominent magnetic anomalies in two narrow intervals between ~304 and 312 mbsf and ~334–351 mbsf were identified. Within these intervals secondary diagenesis resulted in the alteration of ferrimagnetic greigite (Fe_3S_4) to paramagnetic pyrite (FeS_2). This is most likely caused by the accumulation and drainage of fluids, including dissolved methane, and sulfate along high permeability fracture zones. Focused and fault parallel advective fluid flow appears to be limited to the top and brecciated fault zone, and to a slip zone near the subsidiary fault zone, where overlying compacted sediments act as seal that limits further upward fluid migration.

Acknowledgments

This study used samples and data of the International Ocean Discovery Program Expeditions 372 and 375. The authors are grateful to the science party and all technical staff that assisted with the acquisition of samples, data, and contributed in scientific discussions. A.G. acknowledges funding through NWO DeepNL (Grant no. 2018.040), the Korea Institute of Energy Technology Evaluation and Planning (KETEP), and the Ministry of Trade, Industry & Energy (MOTIE) of the Republic of Korea (Grant no. 20168510030830). Lilly Zerbst assisted with early magnetic analyses during tenure of an undergraduate scholarship under the framework of the RISE worldwide program of the German Academic Exchange Service (DAAD). The authors are grateful to Maartje Hamers who assisted with early SEM investigations, Tilly Bouten who produced BSE images on the electron microprobe, Bertwin de Groot who conducted thermomagnetic experiments, Patrick Fulton and Bob Musgrave for reviews on the manuscript.

Data Availability Statement

All shipboard IODP data can be accessed under <https://web.iodp.tamu.edu/LORE/>, all other data presented in this paper are available under (<https://doi.org/10.24416/UU01-XZSKHP>).

References

- Aharon, P., & Fu, B. (2003). Sulfur and oxygen isotopes of coeval sulfate–sulfide in pore fluids of cold seep sediments with sharp redox gradients. *Chemical Geology*, 195(1), 201–218. [https://doi.org/10.1016/S0009-2541\(02\)00395-9](https://doi.org/10.1016/S0009-2541(02)00395-9)
- Barker, D. H. N., Henrys, S., Caratori Tontini, F., Barnes, P. M., Bassett, D., Todd, E., & Wallace, L. (2018). Geophysical constraints on the relationship between seamount subduction, slow slip, and tremor at the North Hikurangi Subduction Zone, New Zealand. *Geophysical Research Letters*, 45(23), 12804–12813. <https://doi.org/10.1029/2018gl080259>
- Bell, R., Holden, C., Power, W., Wang, X., & Downes, G. (2014). Hikurangi margin tsunami earthquake generated by slow seismic rupture over a subducted seamount. *Earth and Planetary Science Letters*, 397, 1–9. <https://doi.org/10.1016/j.epsl.2014.04.005>
- Bottrell, S. H., Parkes, R. J., Cragg, B. A., & Raiswell, R. (2000). Isotopic evidence for anoxic pyrite oxidation and stimulation of bacterial sulphate reduction in marine sediments. *Journal of the Geological Society*, 157(4), 711. <https://doi.org/10.1144/jgs.157.4.711>
- Chang, L., Roberts, A. P., Tang, Y., Rainford, B. D., Muxworthy, A. R., & Chen, Q. (2008). Fundamental magnetic parameters from pure synthetic greigite (Fe_3S_4). *Journal of Geophysical Research*, 113, B06104. <https://doi.org/10.1029/2007jb005502>
- Chen, Y.-H., Chen, Y.-H., Hsu, W.-D., Chang, Y.-C., Sheu, H.-S., Lee, J.-J., & Lin, S.-K. (2019). Using the high-temperature phase transition of iron sulfide minerals as an indicator of fault slip temperature. *Scientific Reports*, 9(1), 7950. <https://doi.org/10.1038/s41598-019-44319-8>
- Coffey, G. L., Savage, H. M., Polissar, P. J., Meneghini, F., Ikari, M. J., Fagereng, Å., et al. (2021). Evidence of seismic slip on a large splay fault in the Hikurangi subduction zone. *Geochemistry, Geophysics, Geosystems*.

- Collett, T. S., Boswell, R., Waite, W. F., Kumar, P., Roy, S. K., Chopra, K., et al. (2019). India National Gas Hydrate Program Expedition 02 Summary of Scientific Results: Gas hydrate systems along the eastern continental margin of India. *Marine and Petroleum Geology*, 108, 39–142. <https://doi.org/10.1016/j.marpetgeo.2019.05.023>
- Cook, A. E., Paganoni, M., Clennell, M. B., McNamara, D., Nole, M., Xiujuan, W., et al. (2020). Physical properties and gas hydrate at a near-seafloor thrust fault, Hikurangi Margin, New Zealand. *Geophysical Research Letters*, 47(16), e2020GL088474. Retrieved from <https://www.essoar.org/doi/10.1002/essoar.10503197.1>
- Crutchley, G. J., Klaeschen, D., Planert, L., Bialas, J., Berndt, C., Papenberg, C., et al. (2014). The impact of fluid advection on gas hydrate stability: Investigations at sites of methane seepage offshore Costa Rica. *Earth and Planetary Science Letters*, 401, 95–109. <https://doi.org/10.1016/j.epsl.2014.05.045>
- Crutchley, G. J., Pecher, I. A., Gorman, A. R., Henrys, S. A., & Greinert, J. (2010). Seismic imaging of gas conduits beneath seafloor seep sites in a shallow marine gas hydrate province, Hikurangi Margin, New Zealand. *Marine Geology*, 272(1), 114–126. <https://doi.org/10.1016/j.margeo.2009.03.007>
- Dekkers, M. J., Passier, H. F., & Schoonen, M. A. A. (2000). Magnetic properties of hydrothermally synthesized greigite (Fe₃S₄)—II. High- and low-temperature characteristics. *Geophysical Journal International*, 141(3), 809–819. <https://doi.org/10.1046/j.1365-246x.2000.00129.x>
- Egli, R. (2013). VARIFORC: An optimized protocol for calculating non-regular first-order reversal curve (FORC) diagrams. *Global and Planetary Change*, 110, 302–320. <https://doi.org/10.1016/j.gloplacha.2013.08.003>
- Ellis, S., Fagereng, A., Barker, D., Henrys, S., Saffer, D., Wallace, L., et al. (2015). Fluid budgets along the northern Hikurangi subduction margin, New Zealand: The effect of a subducting seamount on fluid pressure. *Geophysical Journal International*, 202, 277–297. <https://doi.org/10.1093/gji/ggv12>
- Fagereng, Å., Savage, H. M., Morgan, J. K., Wang, M., Meneghini, F., Barnes, P. M., et al. (2019). Mixed deformation styles observed on a shallow subduction thrust, Hikurangi margin, New Zealand. *Geology*, 47, 872–876. <https://doi.org/10.1130/G46367.1>
- Fagereng, A., & Ellis, S. (2009). On factors controlling the depth of interseismic coupling on the Hikurangi subduction interface, New Zealand. *Earth and Planetary Science Letters*, 278(1), 120–130. <https://doi.org/10.1016/j.epsl.2008.11.033>
- Faure, K., Greinert, J., von Deimling, J. S., McGinnis, D. F., Kipfer, R., & Linke, P. (2010). Methane seepage along the Hikurangi Margin of New Zealand: Geochemical and physical data from the water column, sea surface and atmosphere. *Marine Geology*, 272(1), 170–188. <https://doi.org/10.1016/j.margeo.2010.01.001>
- Fitts, T. G., & Brown, K. M. (1999). Stress-induced smectite dehydration: Ramifications for patterns of freshening and fluid expulsion in the N. Barbados accretionary wedge. *Earth and Planetary Science Letters*, 172(1), 179–197. [https://doi.org/10.1016/S0012-821X\(99\)00168-5](https://doi.org/10.1016/S0012-821X(99)00168-5)
- Fu, Y., von Döbenek, T., Franke, C., Heslop, D., & Kasten, S. (2008). Rock magnetic identification and geochemical process models of greigite formation in Quaternary marine sediments from the Gulf of Mexico (IODP Hole U1319A). *Earth and Planetary Science Letters*, 275(3), 233–245. <https://doi.org/10.1016/j.epsl.2008.07.034>
- Geersen, J., Scholz, F., Linke, P., Schmidt, M., Lange, D., Behrmann, J. H., et al. (2016). Fault zone controlled seafloor methane seepage in the rupture area of the 2010 Maule earthquake, Central Chile. *Geochemistry, Geophysics, Geosystems*, 17(11), 4802–4813. <https://doi.org/10.1002/2016gc006498>
- Greinert, J., Lewis, K. B., Bialas, J., Pecher, I. A., Rowden, A., Bowden, D. A., et al. (2010). Methane seepage along the Hikurangi Margin, New Zealand: Overview of studies in 2006 and 2007 and new evidence from visual, bathymetric and hydroacoustic investigations. *Marine Geology*, 272(1), 6–25. <https://doi.org/10.1016/j.margeo.2010.01.017>
- Greve, A., Kars, M., Zerbst, L., Stipp, M., & Hashimoto, Y. (2020). Strain partitioning across a subduction thrust fault near the deformation front of the Hikurangi subduction margin, New Zealand: A magnetic fabric study on IODP Expedition 375 Site U1518. *Earth and Planetary Science Letters*, 542, 116322. <https://doi.org/10.1016/j.epsl.2020.116322>
- Harrison, R. J., & Feinberg, J. M. (2008). FORCInel: An improved algorithm for calculating first order reversal curve distributions using locally weighted regression smoothing. *Geochemistry, Geophysics, Geosystems*, 9, Q05016. <https://doi.org/10.1029/2008GC001987>
- Holmkvist, L., Kamyshny, A., Vogt, C., Vamvakopoulos, K., Ferdelman, T. G., & Jørgensen, B. B. (2011). Sulfate reduction below the sulfate–methane transition in Black Sea sediments. *Deep Sea Research I: Oceanographic Research Papers*, 58(5), 493–504. <https://doi.org/10.1016/j.dsr.2011.02.009>
- Housen, B. A., & Musgrave, R. J. (1996). Rock-magnetic signature of gas hydrates in accretionary prism sediments. *Earth and Planetary Science Letters*, 139(3), 509–519. [https://doi.org/10.1016/0012-821X\(95\)00245-8](https://doi.org/10.1016/0012-821X(95)00245-8)
- Just, J., Dekkers, M. J., von Döbenek, T., van Hoesel, A., & Bickert, T. (2012). Signatures and significance of aeolian, fluvial, bacterial and diagenetic magnetic mineral fractions in Late Quaternary marine sediments off Gambia, NW Africa. *Geochemistry, Geophysics, Geosystems*, 13(9), Q0A002. <https://doi.org/10.1029/2012GC004146>
- Kars, M., Greve, A., & Zerbst, L. (2019). Occurrence of greigite in gas hydrate-bearing frontal thrust sediments of the Hikurangi margin, New Zealand at site U1518, IODP Expedition 375. San Francisco, CA: AGU.
- Kars, M., & Kodama, K. (2015). Authigenesis of magnetic minerals in gas hydrate-bearing sediments in the Nankai Trough, offshore Japan. *Geochemistry, Geophysics, Geosystems*, 16(3), 947–961. <https://doi.org/10.1002/2014gc005614>
- Kastner, M., Solomon, E. A., Harris, R. N., & Torres, M. E. (2014). Fluid origins, thermal regimes, and fluid and solute fluxes in the forearc of subduction zones. In R. Stein, D. K. Blackman, F. Inagaki, & H.-C. Larsen (Eds.), *Developments in marine geology* (Vol. 7, pp. 671–733). Elsevier.
- Krs, M., Krsová, M., Pruner, P., Zeman, A., Novák, F., & Jansa, J. (1990). A petromagnetic study of Miocene rocks bearing micro-organic material and the magnetic mineral greigite (Sokolov and Cheb basins, Czechoslovakia). *Physics of the Earth and Planetary Interiors*, 63(1), 98–112. [https://doi.org/10.1016/0031-9201\(90\)90064-5](https://doi.org/10.1016/0031-9201(90)90064-5)
- Kuehn, R., Stipp, M., & Leiss, B. (2019). Texture development of clay-rich sediments across the Costa Rica subduction zone. *Journal of Geophysical Research: Solid Earth*, 124, 7756–7770. <https://doi.org/10.1029/2018JB016838>
- Larrasoña, J. C., Roberts, A. P., Musgrave, R. J., Gràcia, E., Piñero, E., Vega, M., & Martínez-Ruiz, F. (2007). Diagenetic formation of greigite and pyrrhotite in gas hydrate marine sedimentary systems. *Earth and Planetary Science Letters*, 261(3), 350–366. <https://doi.org/10.1016/j.epsl.2007.06.032>
- Lauer, R. M., & Saffer, D. M. (2015). The impact of splay faults on fluid flow, solute transport, and pore pressure distribution in subduction zones: A case study offshore the Nicoya Peninsula, Costa Rica. *Geochemistry, Geophysics, Geosystems*, 16(4), 1089–1104. <https://doi.org/10.1002/2014gc005638>
- Liu, D., Li, H., Lee, T.-Q., Sun, Z., Liu, J., Han, L., & Chevalier, M.-L. (2016). Magnetic mineral characterization close to the Yingxiu-Beichuan fault surface rupture zone of the Wenchuan earthquake (Mw 7.9, 2008) and its implication for earthquake slip processes. *Journal of Asian Earth Sciences*, 115, 468–479. <https://doi.org/10.1016/j.jseae.2015.10.019>

- Liu, Q., Roberts, A. P., Larrasoana, J. C., Banerjee, S. K., Guyodo, Y., Tauxe, L., & Oldfield, F. (2012). Environmental magnetism: Principles and applications. *Reviews of Geophysics*, 50(4). <https://doi.org/10.1029/2012RG000393>
- Mau, S., Römer, M., Torres, M. E., Bussmann, I., Pape, T., Damm, E., et al. (2017). Widespread methane seepage along the continental margin off Svalbard—From Bjørnøya to Kongsfjorden. *Scientific Reports*, 7(1), 42997. <https://doi.org/10.1038/srep42997>
- Moore, G. F., Saffer, D., Studer, M., & Costa Pisani, P. (2011). Structural restoration of thrusts at the toe of the Nankai Trough accretionary prism off Shikoku Island, Japan: Implications for dewatering processes. *Geochemistry, Geophysics, Geosystems*, 12, Q0AD12. <https://doi.org/10.1029/2010GC003453>
- Moore, J. C., & Vrolijk, P. (1992). Fluids in accretionary prisms. *Reviews of Geophysics*, 30(2), 113–135. <https://doi.org/10.1029/92RG00201>
- Morgan, J. K., Solomon, E. A., Fagereng, A., Savage, H., Wang, M., Meneghini, F., et al. (2020). *Seafloor Overthrusting at the Hikurangi margin: Ductile Fault Deformation, Fluid Pressures, and Implications for Plate Boundary Processes abstracts, IODP Expeditions 372 & 375 Science Meeting: Creeping Gas Hydrate Slides & Hikurangi Subduction Margin*. New Zealand: Napier.
- Mullender, T. A. T., van Velzen, A. J., & Dekkers, M. J. (1993). Continuous drift correction and separate identification of ferrimagnetic and paramagnetic contributions in thermomagnetic runs. *Geophysical Journal International*, 114(3), 663–672. <https://doi.org/10.1111/j.1365-246X.1993.tb06995.x>
- Musgrave, R. J., Kars, M., & Vega, M. E. (2019). Progressive and punctuated magnetic mineral diagenesis: The rock magnetic record of multiple fluid inputs and progressive pyritization in a volcano-bounded basin, IODP Site U1437, Izu Rear Arc. *Journal of Geophysical Research: Solid Earth*, 124(6), 5357–5378. <https://doi.org/10.1029/2018jb017277>
- Parés, J. M. (2015). Sixty years of anisotropy of magnetic susceptibility in deformed sedimentary rocks. *Frontiers in Earth Science*, 3, 1–13. <https://doi.org/10.3389/feart.2015.00004>
- Passier, H. F., de Lange, G. J., & Dekkers, M. J. (2001). Magnetic properties and geochemistry of the active oxidation front and the youngest sapropel in the eastern Mediterranean Sea. *Geophysical Journal International*, 145(3), 604–614. <https://doi.org/10.1046/j.0956-540x.2001.01394.x>
- Peters, C., & Dekkers, M. J. (2003). Selected room temperature magnetic parameters as a function of mineralogy, concentration and grain size. *Physics and Chemistry of the Earth, Parts A/B/C*, 28(16), 659–667. [https://doi.org/10.1016/S1474-7065\(03\)00120-7](https://doi.org/10.1016/S1474-7065(03)00120-7)
- Pettinga, J. R. (2003). Mud volcano eruption within the emergent accretionary Hikurangi margin, southern Hawke's Bay, New Zealand. *New Zealand Journal of Geology and Geophysics*, 46(1), 107–121. <https://doi.org/10.1080/00288306.2003.9514999>
- Pike, C. R., Roberts, A. P., & Verosub, K. L. (1999). Characterizing interactions in fine magnetic particle systems using first order reversal curves. *Journal of Applied Physics*, 85(9), 6660–6667. <https://doi.org/10.1063/1.370176>
- Roberts, A. P. (1995). Magnetic properties of sedimentary greigite (Fe₃S₄). *Earth and Planetary Science Letters*, 134, 227–236.
- Roberts, A. P., Chang, L., Rowan, C. J., Horng, C.-S., & Florindo, F. (2011). Magnetic properties of sedimentary greigite (Fe₃S₄): An update. *Reviews of Geophysics*, 49, RG1002. <https://doi.org/10.1029/2010rg000336>
- Roberts, A. P., Heslop, D., Zhao, X., & Pike, C. R. (2014). Understanding fine magnetic particle systems through use of first-order reversal curve diagrams. *Reviews of Geophysics*, 52(4), 557–602. <https://doi.org/10.1002/2014rg000462>
- Roberts, A. P., Liu, Q., Rowan, C. J., Chang, L., Carvallo, C., Torrent, J., & Horng, C.-S. (2006). Characterization of hematite (α-Fe₂O₃), goethite (α-FeOOH), greigite (Fe₃S₄), and pyrrhotite (Fe₇S₈) using first-order reversal curve diagrams. *Journal of Geophysical Research*, 111, B12S35. <https://doi.org/10.1029/2006JB004715>
- Roberts, A. P., Pike, C. P., & Verosub, K. L. (2000). First-order reversal curve diagrams: A new tool for characterizing the magnetic properties of natural samples. *Journal of Geophysical Research*, 105, 28461–28457.
- Roberts, A. P., & Weaver, R. (2005). Multiple mechanisms of remagnetization involving sedimentary greigite (Fe₃S₄). *Earth and Planetary Science Letters*, 231(3), 263–277. <https://doi.org/10.1016/j.epsl.2004.11.024>
- Rowan, C. J., Roberts, A. P., & Broadbent, T. (2009). Reductive diagenesis, magnetite dissolution, greigite growth and paleomagnetic smoothing in marine sediments: A new view. *Earth and Planetary Science Letters*, 277(1), 223–235. <https://doi.org/10.1016/j.epsl.2008.10.016>
- Ruppel, C. D., & Waite, W. F. (2020). Timescales and processes of methane hydrate formation and breakdown, with application to geologic systems. *Journal of Geophysical Research: Solid Earth*, 125(8), e2018JB016459. <https://doi.org/10.1029/2018JB016459>
- Saffer, D. M. (2015). The permeability of active subduction plate boundary faults. *Geofluids*, 15(1–2), 193–215. <https://doi.org/10.1111/gfl.12103>
- Saffer, D. M., & Sreaton, E. J. (2003). Fluid flow at the toe of convergent margins: interpretation of sharp pore-water geochemical gradients. *Earth and Planetary Science Letters*, 213(3), 261–270. [https://doi.org/10.1016/S0012-821X\(03\)00343-1](https://doi.org/10.1016/S0012-821X(03)00343-1)
- Saffer, D. M., & Tobin, H. J. (2011). Hydrogeology and mechanics of subduction zone forearcs: fluid flow and pore pressure. *Annual Review of Earth and Planetary Sciences*, 39(1), 157–186. <https://doi.org/10.1146/annurev-earth-040610-133408>
- Saffer, D., Wallace, L., & Petronotis, K. (2017). *Expedition 375 scientific prospectus: Hikurangi subduction margin coring and observatories*. International Ocean Discovery Program. <http://dx.doi.org/10.14379/iodp.sp.375.2017>
- Sreaton, E., Kimura, G., Curewitz, D., Moore, G., Chester, F., Fabbri, O., et al. (2009). Interactions between deformation and fluids in the frontal thrust region of the NanTroSEIZE transect offshore the Kii Peninsula, Japan: Results from IODP Expedition 316 Sites C0006 and C0007. *Geochemistry, Geophysics, Geosystems*, 10(12). <https://doi.org/10.1029/2009gc002713>
- Skarbek, R. M., & Saffer, D. M. (2009). Pore pressure development beneath the décollement at the Nankai subduction zone: Implications for plate boundary fault strength and sediment dewatering. *Journal of Geophysical Research*, 114, B07401. <https://doi.org/10.1029/2008jb006205>
- Snowball, I. F. (1991). Magnetic hysteresis properties of greigite (Fe₃S₄) and a new occurrence in Holocene sediments from Swedish Lapland. *Physics of the Earth and Planetary Interiors*, 68(1), 32–40. [https://doi.org/10.1016/0031-9201\(91\)90004-2](https://doi.org/10.1016/0031-9201(91)90004-2)
- Suess, E. (2010). Marine cold seeps. In K. N. Timmis (Ed.), *Handbook of hydrocarbon and lipid microbiology* (pp. 185–203). Berlin, Heidelberg: Springer Berlin Heidelberg.
- Taira, A., Hill, I., Firth, J., Berner, U., Brückmann, W., Byrne, T., et al. (1992). Sediment deformation and hydrogeology of the Nankai Trough accretionary prism: Synthesis of shipboard results of ODP Leg 131. *Earth and Planetary Science Letters*, 109(3), 431–450. [https://doi.org/10.1016/0012-821X\(92\)90104-4](https://doi.org/10.1016/0012-821X(92)90104-4)
- Torres, M. E., Cox, T., Hong, W. L., McManus, J., Sample, J. C., Destrigneville, C., et al. (2015). Crustal fluid and ash alteration impacts on the biosphere of Shikoku Basin sediments, Nankai Trough, Japan. *Geobiology*, 13(6), 562–580. <https://doi.org/10.1111/gbi.12146>
- Torres, M. E., Teichert, B. M. A., Tréhu, A. M., Borowski, W., & Tomaru, H. (2004). Relationship of pore water freshening to accretionary processes in the Cascadia margin: Fluid sources and gas hydrate abundance. *Geophysical Research Letters*, 31, L22305. <https://doi.org/10.1029/2004gl021219>

- van Baak, C. G. C., Vasiliev, I., Palcu, D. V., Dekkers, M. J., & Krijgsman, W. (2016). A greigite-based magnetostratigraphic time frame for the Late Miocene to recent DSDP Leg 42B cores from the Black Sea. *Frontiers in Earth Science*, 4(60). <https://doi.org/10.3389/feart.2016.00060>
- Van Baak, C. G. C., Vasiliev, I., Stoica, M., Kuiper, K. F., Forte, A. M., Aliyeva, E., & Krijgsman, W. (2013). A magnetostratigraphic time frame for Plio-Pleistocene transgressions in the South Caspian Basin, Azerbaijan. *Global and Planetary Change*, 103, 119–134. <https://doi.org/10.1016/j.gloplacha.2012.05.004>
- Vasiliev, I., Franke, C., Meeldijk, J. D., Dekkers, M. J., Langereis, C. G., & Krijgsman, W. (2008). Putative greigite magnetofossils from the Pliocene epoch. *Nature Geoscience*, 1(11), 782–786. <https://doi.org/10.1038/ngeo335>
- Wallace, L. M., Saffer, D. M., Barnes, P. M., Pecher, I. A., Petronotis, K. E., LeVay, L. J., et al. (2019). Hikurangi subduction margin coring, logging, and observatories. Proceedings of the International Ocean Discovery program. College Station, TX: International Ocean Discovery Program. <https://doi.org/10.14379/iodp.proc.372B375.2019>
- Wallace, L. M., Webb, S. C., Ito, Y., Mochizuki, K., Hino, R., & Henrys, S. (2016). Slow slip near the trench at the Hikurangi subduction zone, New Zealand. *Science*, 352(6286), 701–704. <https://doi.org/10.1126/science.aaf2349>
- Watson, S. J., Mountjoy, J. J., Barnes, P. M., Crutchley, G. J., Lamarche, G., Higgs, B., et al. (2019). Focused fluid seepage related to variations in accretionary wedge structure, Hikurangi margin, New Zealand. *Geology*, 48(1), 56–61. <https://doi.org/10.1130/g46666.1>
- Yang, T., Chou, Y.-M., Ferré, E. C., Dekkers, M. J., Chen, J., Yeh, E.-C., & Tanikawa, W. (2020). Faulting processes unveiled by magnetic properties of fault rocks. *Reviews of Geophysics*, 58(4), e2019RG000690. <https://doi.org/10.1029/2019RG000690>
- Yang, T., Dekkers, M. J., & Chen, J. (2018). Thermal alteration of pyrite to pyrrhotite during earthquakes: New evidence of seismic slip in the rock record. *Journal of Geophysical Research: Solid Earth*, 123(2), 1116–1131. <https://doi.org/10.1002/2017jb014973>
- Yang, T., Dekkers, M. J., & Zhang, B. (2016). Seismic heating signatures in the Japan Trench subduction plate-boundary fault zone: evidence from a preliminary rock magnetic 'geothermometer'. *Geophysical Journal International*, 205(1), 332–344. <https://doi.org/10.1093/gji/ggw013>
- Yang, T., Mishima, T., Ujiie, K., Chester, F. M., Mori, J. J., Eguchi, N., & Toczko, S. (2013). Strain decoupling across the décollement in the region of large slip during the 2011 Tohoku-Oki earthquake from anisotropy of magnetic susceptibility. *Earth and Planetary Science Letters*, 381, 31–38. <https://doi.org/10.1016/j.epsl.2013.08.045>
- You, K., Flemings, P. B., Malinverno, A., Collett, T. S., & Darnell, K. (2019). Mechanisms of methane hydrate formation in geological systems. *Reviews of Geophysics*, 57(4), 1146–1196. <https://doi.org/10.1029/2018RG000638>